Structural, topological, dielectric, and electrical properties of a novel calcium bismuth tungstate ceramic for some device applications

Sudhansu Sekhar Hota[1], Debasish Panda[1,*] , and Ram Naresh Prasad Choudhary[1]

[1] *Department of Physics, Multifunctional Research Laboratory, Siksha 'O' Anusandhan (Deemed to Be University), Bhubaneswar 751030, India*

ABSTRACT

This article describes the characterization (structural, topological, dielectric, and electrical properties) of a lead-free complex perovskite $Ca_3Bi_2WO_9$ (CBWO) prepared by a solid-state reaction method. The room-temperature X-ray structural analysis of the material suggests crystallization of the material in monoclinic crystal symmetry with average crystallite size and lattice strain of 73.29 nm and 0.0023, respectively. Studies of microstructural and compositional properties of the sample using scanning electron microscopy (SEM) and EDX (energy-dispersive analysis X-ray) revealed the good quality of the sample (uniformity and compactness of grains and grain boundary). A careful examination of the temperature and frequency dependence of the impedance, dielectric, and ac conductivity characteristics of the material shows the existence of large dielectric dispersion, relaxation mechanisms, and a non-Debye type of conduction mechanism in it. The diminishing of resistance or radius of semicircular arcs in Nyquist plots and impedance analysis show the semiconductor behavior of the material. Fitted parameters obtained using ZSIMPWIN software also support this nature. The nature of field-dependent polarization [hysteresis loops (P–E)] shows that ferroelectricity may exist in the sample. The negative temperature coefficient of resistance (NTCR) character, which applies to NTC thermistor application, is shown by calculating the temperature coefficient of resistance (TCR) and thermistor constant (β).

Address correspondence to E-mail: pandadebasish9078@gmail.com

1 Introduction

Ferroelectric materials and equipments take part in the production of different types of devices in the area of device engineering, for example, in actuators, printing devices, super-capacitors, dynamic non-volatile memory (RAM), ultrasonic transducers, and electro-optic detectors [1, 2]. Several bulk ferroelectric materials are extensively studied for their distinctive features, such as electro-mechanical coupling factor, high dielectric constant, and a piezoelectric coefficient useful for devices [3, 4]. The advancement of relaxor materials and lead-free ferroelectrics as opposed to lead-based ferroelectrics is now in high demand for device manufacturing. The toxicity of lead is the main reason for the getaway of lead-based perovskites for the fabrication of devices. To that end, the World Forum has adopted many directives, including 2002/95/EC and 2002/96/EC, to limit the utilization of lead-based gadgets in the future [5]. The processing and degrading of lead-based gadgets cause severe concern for human health and global pollution. Considering the problems, major efforts are being made to create new materials which are lead-free a choice. Then, in 1949, the bismuth layer-structured ferroelectric (BLSF) of the Aurivillius family was discovered to fabricate a lead-free material with ferroelectric uniqueness [6]. Since then, numerous (BLSF) materials of the family were reported for the purpose [7]. Researchers have now carved a large number of compounds in the Aurivillius family due to their outstanding switching speed, high retentivity, minimal leakage current density, and low working voltage [8].

The Aurivillius family consists of $[Bi_2O_2]^{2+}$ layers with perovskite $[A_{n-1}B_nO_{3n+1}]^2$. Normally 'A' is a mono, di, or trivalent cation, which has dodecahedral coordination, and 'B' is a transition element that has octahedral coordination and denotes the number of perovskite-like slabs [9]. The significance of the bismuth layer in identifying the electric and ferroelectric characteristics of these materials has been discovered [10]. The bismuth layer is said to be paraelectric, whereas perovskite unit cell structures are ferroelectric. As a result, doping in these multilayer ceramics to raise their characteristics has grabbed the attention of researchers. These bismuth-layered structure ferroelectrics (BLSFs) and their solid solutions are the better promising materials for use in ferroelectric random access memory (FeRAMs) [11]. The influence of the A- and B-site replacements in these materials on their physical and chemical characteristics have been generally to be useful. Several ways have also been generally employed to increase the performance of such types of ferroelectrics. Over the last few decades, researchers have been eager to learn more about the novel features indicated in perovskite-type materials [12]. Sun et.al have reported the approaches to building a neural network and the potential applications of ABO_3-type multiferroic perovskite materials in hardware artificial intelligence systems [13]. These classes of materials have distinctive electrostriction, ferroelectric, pyroelectric, and piezoelectric capabilities allowing them to perform realistically as passive components in a variety of modern appliances [14]. Due to the extraordinary resistive and electric properties, the synthesis of lead zirconium titanate $(Pb(ZrTi)O_3 = PZT)$ series including barium titanate $(BaTiO_3 = BTO)$ and calcium titanate $(CaTiO_3 = CTO)$ perovskite materials has many applications in the industry. CTO types of materials were considered for their potential application as phosphors, adsorbents, catalysts, and promoters of integration of titanium implants with bone. These materials were synthesized via solid-state method, wet chemical pathways, and other physical procedures. Moreover, such type of materials also has applications in dye-sensitized solar cells, piezoelectric ceramics, low-temperature ferroelectric epitaxial layers, and improved electrochemical sensors/biosensors [15].

Moving on, we turn our attention to double perovskite, which has amazing properties and is now the focus of the present study. $A_2B_2O_6$ is a common formula for double perovskite, where A- and B-sites can be considered host matrices, yielding a new structure as $AA'BB'O_6$ where A and B are filled by foreign cations [16]. When two dopants derived from alkali metals, alkaline-earth metals, and rare-earth elements are shared by the A- and B-sites of a double perovskite, fresh unique features emerge. The double perovskites have fresh unique features like stability, tunable properties, and also massive potential leading to extraordinary performance, which is used as an environmentally friendly optoelectronic device [17]. The synthesis of perovskite materials has fascinated researchers in recent years because of its supremacy in the field of lithium-ion battery devices, photoluminescence, photocatalytic, super-capacitors, welding, and capacitors [18–23].

Furthermore, the present research is mostly devoted to examine several perovskites to improve their multifunctional characteristics. As a result, the current study is primarily focused on the synthesis and characterization of a triplet perovskite by combining two non-perovskite materials or exchanging an element of one with the other. So a two-layer Aurivillius phase ferroelectric ceramic, $A_3Bi_2BO_9$ (A symbolizes the A-site cation), has piqued the interest of both technological and scientific researchers due to its amazing overall performance, which has pushed it into the spotlight of the current study. The typical formula of the layered ferroelectrics (LFE) with multiple perovskite structures can be written as $A_{m-1}Bi_2B_mO_{3m+3}$, where A = Ca^{2+}, Pb^{2+}, Sr^{2+}, Ba^{2+}, Na^+, K^+, and B = W^{6+}, Ti^{4+}, Fe^{3+}, Ta^{5+}, and different ions configured to fit into the oxygen octahedrons [24]. Researchers have discovered several members of the Aurivillius family. Durán-Martín et al. [25] studied the influence of the Bi-site substitution on the ferroelectricity of one of the Aurivillius compounds $Bi_2SrNb_2O_9$. Susan et al. [26] reported that $Bi_2SrNb_2O_9$ has cation disorder with a more distorted niobium octahedral environment as compared to that of the $Bi_2SrTa_2O_9$ model. Jae-Hyun et al. [27] have reported the synthesis, structure, and optical properties of two new perovskites: $Ba_2Bi_{2/3}TeO_6$ and $Ba_3Bi_2TeO_9$. Moure et al. [28] have investigated texture and the microstructure dependence of the dielectric properties with some exceptions. The dc conductivity of the Bi_3TiNbO_9 ceramic, formed by natural sintering and hot pressing from amorphous precursors, has also been discussed in the study. Wang et al. [29] reported the electrical transport, magnetic, and thermoelectric behavior of a series of Fe, Mn, and Cu-doped $Ca_3Co_4O_9$. Xinchun et al. [30] have reported the better electrical behavior of $CaBi_2Nb_2O_9$-based Aurivillius piezoceramics via structural distortion. Hepeng et al. [31] studied the lead-free $Ca_{1-x}Ce_xBi_2Nb_{1.975}(Cu_{0.25}W_5)_{0.025}O_9$ (CBNCW-xCe: x = 0.00, 0.02, 0.04, 0.06, and 0.09) to find out piezoelectric properties. To the best of our knowledge, there is no direct information in the literature regarding any phase of the CBWO system. This has motivated us to learn various properties of the solid-state reaction method that prepared the CBWO system to illustrate the structures with electronic properties.

CBWO is also prepared by adding two other non-perovskite/layer compounds, such as $Ca_2Bi_2O_5$ and $CaWO_4$, or by replacing a few elements from one to the other. However, when these two compounds are combined, they show distinct properties and characteristics from CBWO. As a result, it was synthesized as a single compound, and the relation between structural variation and electrical characteristics (dielectric property, ferroelectric property) was systematically examined with some device applications.

2 Experimental approach

A conventional high-temperature solid-state reaction technique was used to create a polycrystalline sample of complex calcium bismuth tungstate (CBWO). A digital balance (MODEL: ML204/A01) with an accuracy of up to 0.0001 was used to calculate the stoichiometric ratio of metal oxides and carbonates to prepare the material. The materials utilized are calcium carbonate ($CaCO_3$), bismuth oxide (Bi_2O_3), and tungsten oxide (WO_3) (M/S- Loba Chemie Pvt. Ltd.)(Purity (99%)), satisfying a chemical equation given below:

$$3CaCO_3 + Bi_2O_3 + WO_3 \rightarrow Ca_3Bi_2WO_9 + 3CO_2.$$
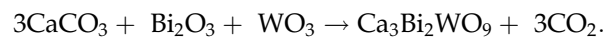
The required amount of the constituent compounds was grounded for 2 h in a dry (air) medium and 3 h in a wet (methanol) medium using a mortar and pestle. The ground fine homogenous powder was calcined at 850 °C (with a heating rate of 3 °C/min) for 5 h in a programmable furnace to make the compound. The preliminary structure of calcinated sample was investigated by an X-ray powder diffractometer (Model: Rikagu ultima Japan) with a CuK_α ($\lambda = 1.5405$ Å) radiation source across a wide range of Bragg's angles ($20^0 \leq 2\theta \leq 80^0$) to confirm the creation of the required material. The crystal system, unit cell parameters, and peak Miller indices were all estimated using the computer program "EXPO 2014" [32]. Then under a hydraulic pressure of 4×10^6 N/m², the calcined powder was used to make cylindrical-shaped pellets of thickness 1–2 mm and diameter 12 mm using polyvinyl alcohol as a binder. The pellets were sintered at 930 °C for 5 h to make a high density of the sample. The geometrical density of the synthesized compound was calculated to be 5.4807 g/cm³.

SEM-EDAX was used for microstructural and compositional analysis of the sample. To study the electrical properties, two surfaces of the pellet were coated with silver paint and dried at 125 °C. An LCR

analyzer (Model: N4L PSM, 1735) was used to study dielectric and the electrical characteristics of the sample at various frequencies (10 kHz-1 MHz) and temperatures (25–500 °C). The ferroelectric hysteresis loops (P-E) were traced using a P–E loop tracer (M/S-Marine, India) (Radiant technology version 4.8.0) at different temperatures.

3 Consequences and discussion

3.1 Structural and morphological studies

Figure 1a displays the X-ray powder diffraction (XRD) pattern of the calcined CBWO powder at room temperature. As the fabricated new compound has no prior structural information, most of the prominent reflection peaks of the pattern were used to carry out structural analysis using various computer
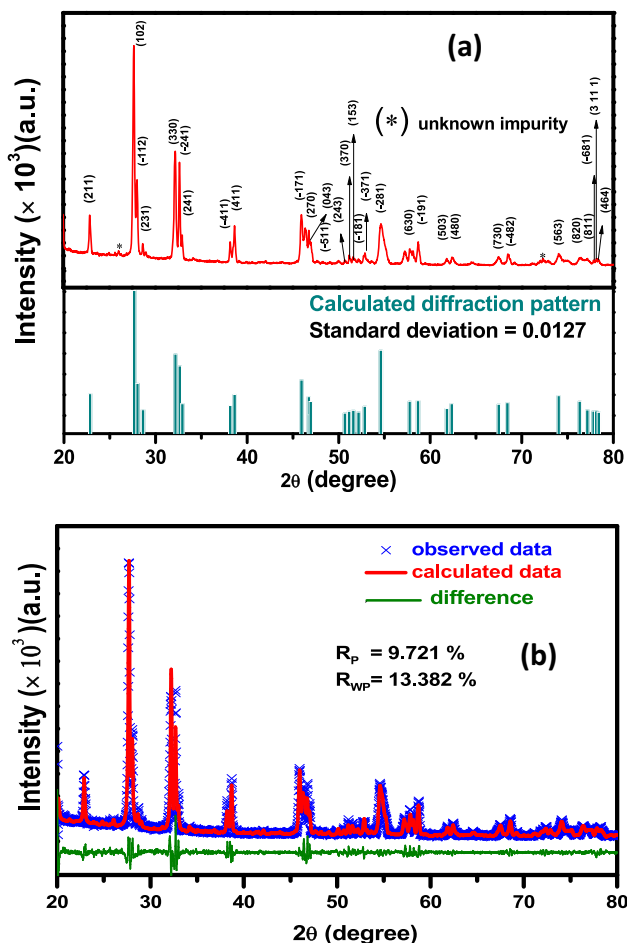

Fig. 1 **a** X-ray diffraction pattern of $Ca_3Bi_2WO_9$ and **b** Rietveld refinement of $Ca_3Bi_2WO_9$

software such as POWD-MULT, FullProf Suite, X´Pert HighScore Plus, MAUD, GSAS II etc. Each one has given different results, which were not consistence with the synthesis process (including ingredients), and physical properties of the prepared material. Finally, the structural and refinement parameters, obtained by computerized software EXPO 2014, were found to be consistent with the physical properties of the material and, thus, acceptable. From the best structural parameters fit, the final structural parameters (lattice dimensions) were determined to have the smallest standard deviation (of 0.01278) and best fit. The structural analysis shows the creation of a single-phase monoclinic crystal structure of the material. The indexed peaks are shown in Fig. 1(a), whereas Fig. 1(b) represents the Rietveld refinement (with XRD data) of the CBWO ceramic. For Rietveld refinement, the Le-Bail technique is adopted for EXPO 2014 program having reliability factors (using Pseudo-Voigt function); $R_p = 9.721\%$, $R_{wp} = 13.382\%$, $R_e = 0.009\%$ with calculated parameters; cell parameters a = 10.0987 Å, b = 14.6952 Å, c = 6.8318 Å, cell volume (V) = 1013.68 $(Å)^3$, β = 91.104°. The structural analysis of the material with a large number of reflections (particularly of a single crystal or methods) is expected to provide new and more accurate data. The homogeneous arrangement of grains with precise grain boundaries could be revealed by SEM (scanning electron microscope).

The SEM micrograph of the prepared CBWO ceramic is revealed in Fig. 2a. The existence of tightly filled grains with tiny voids simplifies the creation of dense material. A deformed polycrystalline material is shown by the formation of regular distribution of grains with varied sizes and shapes. The EDX picture of CBWO ceramic is shown in Fig. 2b. The study of the EDX picture (Fig. 2c) shows the presence of all component elements (Ca, Bi, W, O) in weight proportion. The grain distribution curve is shown here where grain diameter (μm) is taken along the x-axis and counts in percentage (number of particles) are taken along the y-axis. The ImageJ program is used to conclude the number of particles and their grain size. The average grain size is calculated to be 0.86 μm after plotting the histogram.

The occurrence of wide-width peaks in the XRD pattern is associated with lattice strain of distorted form of structure. The Williamson and Hall (W–H) plotting method relies on calculating the peak width
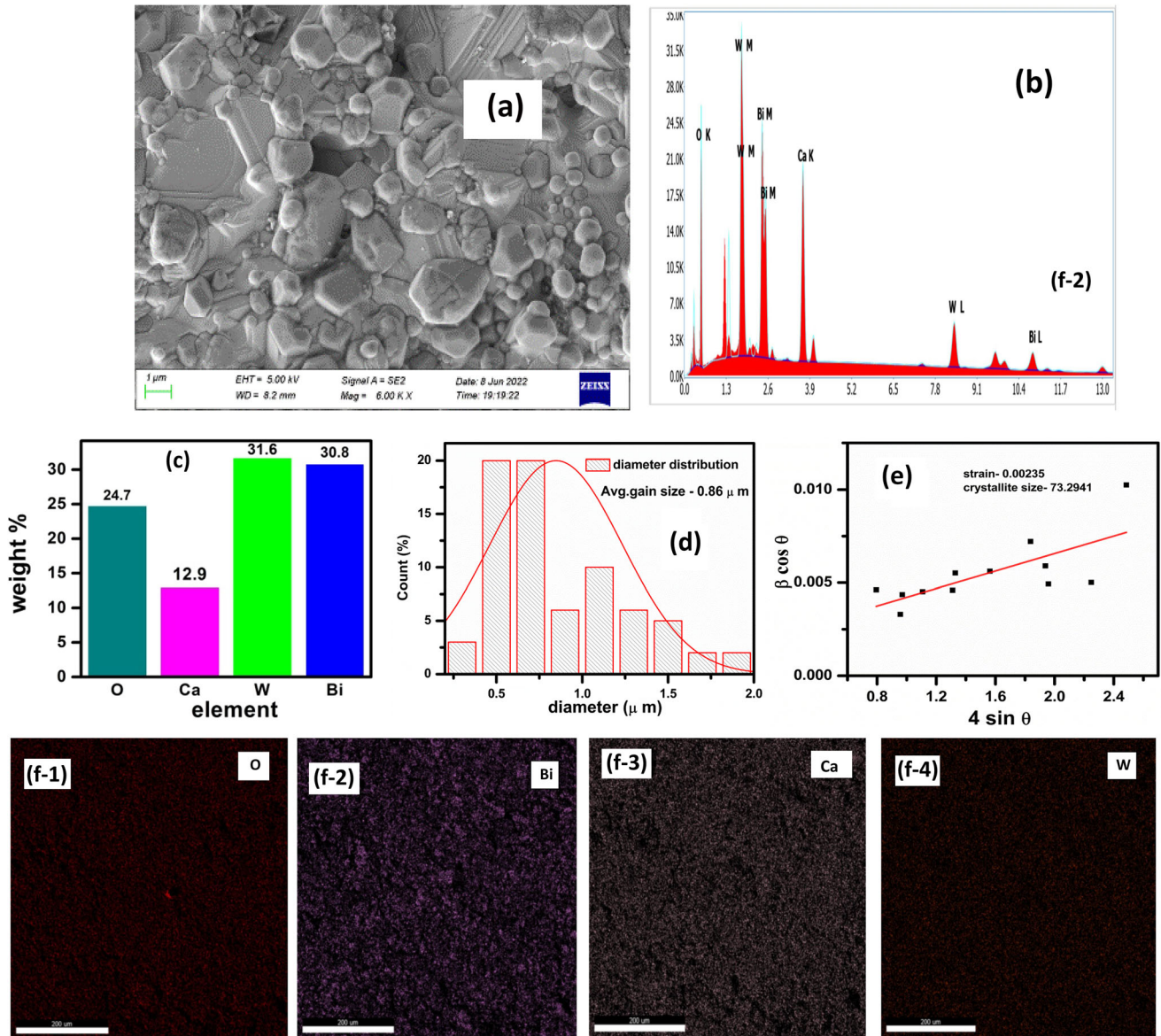
Fig. 2 a SEM micrograph, **b** display of EDX picture of $Ca_3Bi_2WO_9$, **c** histogram plot of weight% of the element, **d** diameter distribution curve, **e** W–H plots and **f** O, Bi, Ca, and W elements of the compound across the full cross section

as a function of 2θ. They give a relation for estimation of average crystallite size and lattice strain, such as $\beta cos\theta = 4\varepsilon sin\theta + k\lambda/D$, where θ = angle of diffraction, β is the FWHM (full width at Half maxima), $k = 0.89$, and ε = lattice strain, λ is the wavelength have value 0.154 nm, and D denotes average crystallite size. For this reason, a plot is drawn by choosing $4sin\theta$ on the x-axis and $\beta cos\theta$ on the y-axis (Fig. 2.e). The slope of the curve gives the lattice strain, whereas the y-intercept represents average crystallite size. In this work, the average crystallite size is approximately 73.29 nm,

and the strain is about 0.0023 [33]. The energy-dispersive spectra (EDS) of CBWO are depicted in Fig. 2f, revealing a consistent distribution of elements over the whole cross section of the sample with an appropriate stoichiometric ratio.

3.2 Topological studies

Figure 3a, b shows three-dimensional topographic pictures generated by the mountainslab computerized program, with high-intensity grains and voids visible on the surface of CBWO, indicating surface roughness. The surface roughness is calculated from
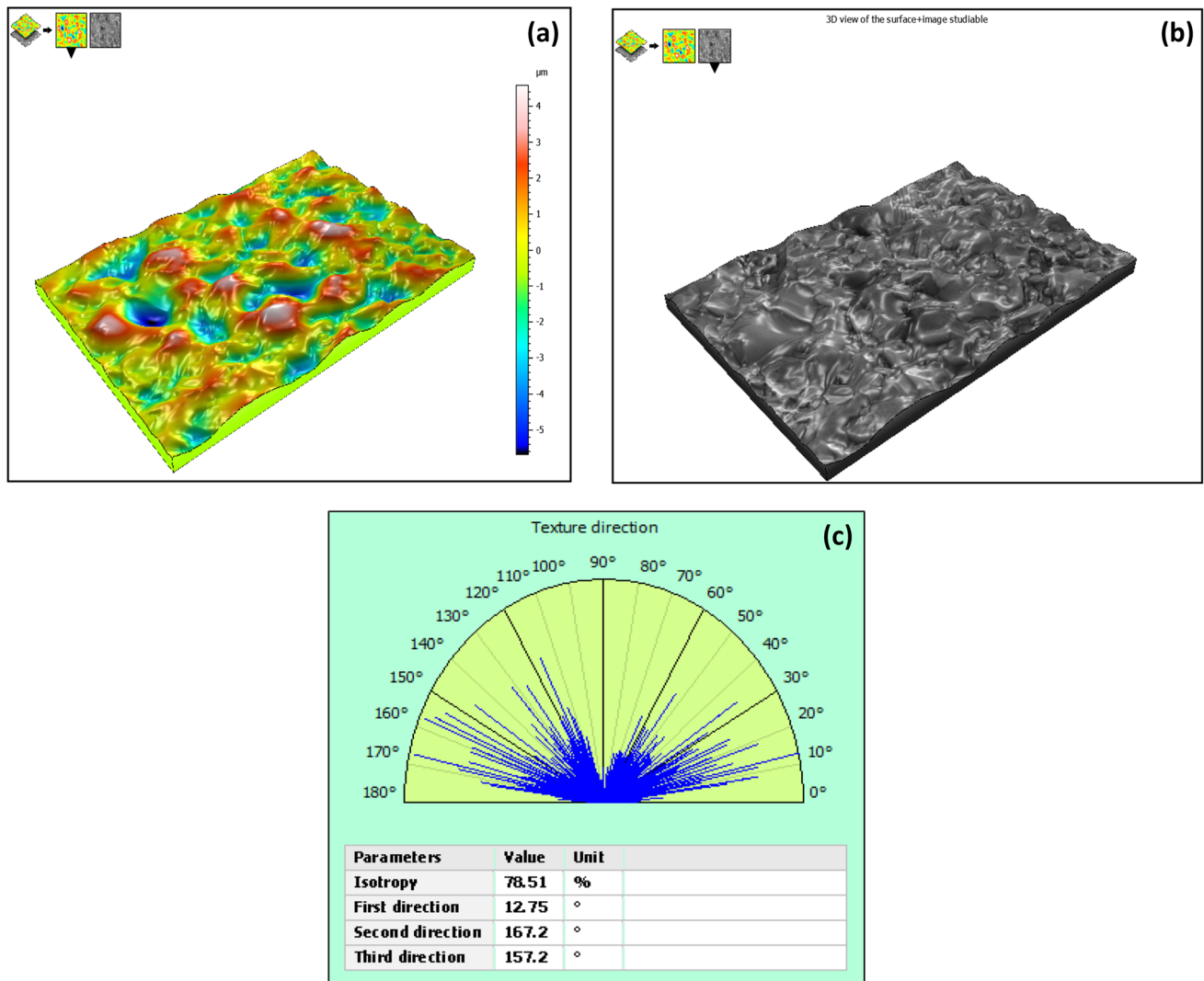
Parameters	Value	Unit
Isotropy	78.51	%
First direction	12.75	°
Second direction	167.2	°
Third direction	157.2	°

Fig. 3 **a** Topography of SEM, **b** 3D view of compact surface (**c**) the polar graph with texture direction

this topography using the ISO25178 characteristics of a scale-limited surface, as shown in Table 1 [34].

$$S_q = \sqrt{\frac{1}{A} \iint_A Z^2(x,y)dxdy}\ S_{sk}$$

$$= \frac{1}{S_q^3}\left[\frac{1}{A}\iint_A Z^3(x,y)dxdy\right]\quad S_a$$

$$= \frac{1}{A}\iint_A |Z(x,y)|dxdy$$

S_q denotes the root-mean-square height. The highest peak height is denoted by Sp. The maximum pit height, the maximum height of the scale-limited surface, and the arithmetical mean height of the material are denoted by *Sv, Sz, and Sa*, respectively. *Ssk* (skewness) and *Sku* (kurtosis) calculate the mean cube and mean quartic values of the ordinate values, respectively. The polar graph with texture directions is depicted in Fig. 3c [35]. In general, isotropy has

Table 1 Parameters of surface roughness

Symbolized parameters	Values
Sq	28.77 (nm)
Sp	239.8 (nm)
Sv	159.5 (nm)
Sz	399.3 (nm)
Sa	21.90 (nm)
Ssk	− 0.3666
Sku	4.502

features that are independent or comparable in all directions. In the polar diagram, the isotropy value of 78.51% may provide a regular orientation of grain texture and compactness on the surface of CBWO ceramic.

3.3 Dielectric spectroscopy

The dielectric constant or dielectric permittivity of the material is a characteristic of a material, which is used to evaluate the capacity to hold energy from an applied electric field. It is defined as the ratio of vacuum field strength to material medium field strength with an equivalent quantity of charge dispersal. Charges move up from atoms and molecules inside the material and vibrate in response to the applied field. The vibration of the atoms or molecules in materials causes the charged ions to be displaced from their equilibrium location, increasing polarization.

Figure 4a presents the relation of relative dielectric permittivity (ε_r) with frequency in the temperatures range from 25 to 500 °C. In the low-frequency zone, a widely discrete value of dielectric permittivity is seen because of the occurrence of ionic, dipolar/ orientational space /interfacial charge, and electronic polarization together [36].

In the high-frequency zone, both the tangent loss and dielectric permittivity decrease and attain a steady value. Such characteristics demonstrate that in the low-frequency zone, every type of polarization, particularly space/interfacial polarization, contributes to high permittivity. At high frequencies, electronic polarization is depleted, ensuing in a decrease in tangent loss and dielectric constant [37]. The increased permittivity value in the low-frequency zone may be represented using the Maxwell–Wagner model of space charge polarization [38], which also agrees with the theory of Koop's model [36, 38].

According to the model, the dielectric medium has two parts: low-conducting grain boundaries at the low-frequency zone and high-conducting grain boundaries at the high-frequency zone. At high frequencies, electrons follow the hopping process with a rapidly varying field [39], and they must flow within grains and across grain boundaries because resistance is large at grain boundaries. Space charge accumulates at low frequencies, which raises permittivity. However, at a high frequency, the dielectric permittivity decreases when the space charge is discharged. The grain boundary performs like a Schottky-like barrier because of its deviation in the work function of charge carriers in the grain and grain

Fig. 4 **a** Relation of frequency against dielectric permittivity, **b** tan delta with frequency, **c** dielectric permittivity with temperature, and (d) tan delta with a temperature of $Ca_3Bi_2WO_9$
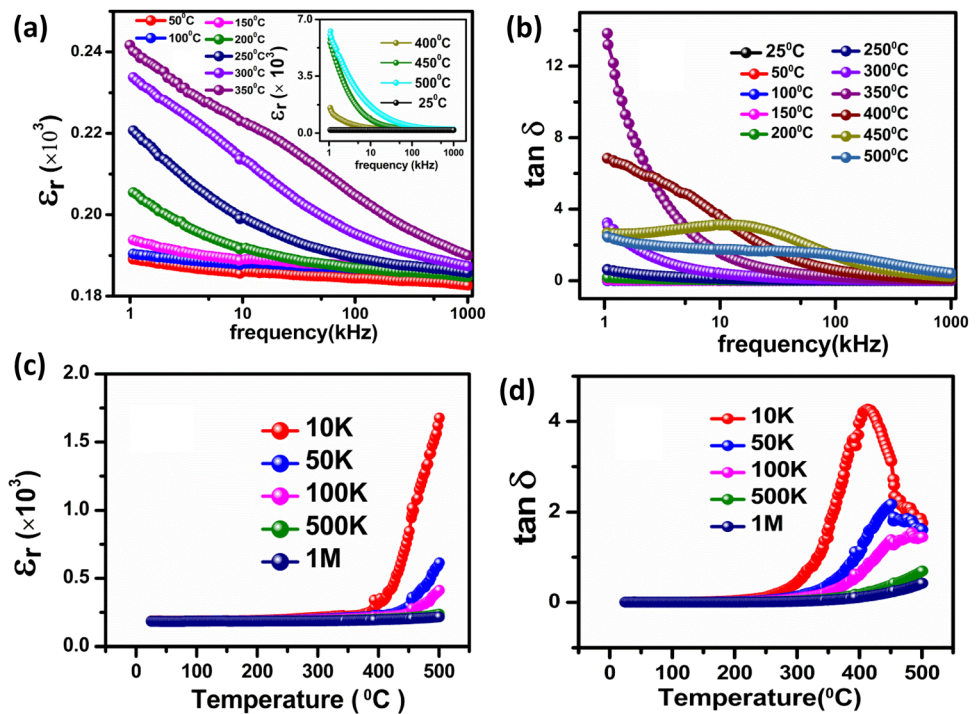
boundary area. On apply of electric current over the grain boundary region, the free charge carriers are collected at the grain–grain boundary interfaces, and a non-Debye-like relaxation is detected beneath the applied field [40–43].

The dielectric loss part (tan δ) shows energy dissipation and detects defects, impurities, and imperfections under the influence of an alternating current field [44]. The variation of dielectric loss with the frequency of the synthesized material at several temperatures is depicted in Fig. 4(b). Dielectric loss exhibits the same behavior as dielectric permittivity. At low frequencies, the dipoles are misaligned about the applied electric field, and a high value of the tan δ is predicted. The dielectric loss in the high-frequency zone decreases because of reduced thermal agitation and misalignment. Dielectric permittivity relation with temperature is shown in Fig. 4 (c), whereas dielectric loss with temperature is shown in Fig. 4 (d) for frequencies of 10 kHz, 50 kHz, 100 kHz, 500 kHz, and 1 MHz. The measurement of permittivity and loss is highly dependent on the probe. The dielectric constant and the dielectric loss equivalent to each frequency remain constant at low temperatures and gradually rise as temperature increases. The tangent loss and dielectric constant at low temperatures may due to the inactive activity of mobile electrons and polarons. At high temperatures, the high value of both the tangent loss and the dielectric constant could be attributable to the activation of electron hopping (because of lattice vibration in materials), which causes the polaron hopping mechanism [45].

3.4 AC conductivity

The applied external field controls the movement of charge carriers (electrons/holes), which is important for the conduction process of the sample. The higher dc conductivity value is due to free charges in the substance. Ionic charges are utilized in the hopping mechanism, whereas electronic charges are inactive mobile carriers. As a result, the conduction process is caused by hopping among nearby donors and acceptors.

The total conductivity (σ) is considered by the relation:

$$\sigma = \frac{t}{A}\left[\frac{Z'}{Z'^2 + Z''^2}\right],$$

where t is the thickness and A is the surface area of the pellet.

Figure 5a shows the ac conductivity vs. frequency at various temperatures. The ac conductance is calculated from the relation: $\sigma_{ac} = \omega\varepsilon_r\varepsilon_0 tan\delta = 2\pi f\varepsilon_r\varepsilon_0 tan\delta$, where f denotes the linear frequency of the applied ac field, $\omega = 2\pi f$ as the angular frequency, ε_0 is called as permittivity in a vacuum, ε_r is known as dielectric permittivity, and tan δ presents dielectric loss/tangent loss. The activities of ac conductance (σ_{ac}) can be understood from Jonscher's Power Law (JPL) through universal dielectric response (UDR) [46, 47];

$$\sigma_{total}(\omega) = \sigma_{dc} + A(T)\omega^S,$$

where $\sigma_{total}(\omega)$ represents the total conductivity, σ_{dc} presents the dc conductivity, $\sigma_{ac}(\omega)$ indicates the ac conductivity, A(T) represents the pre-exponential factor, ω is the angular frequency and s is the exponential power. At low frequencies, the fitted ac conductivity plot displays a broadly scattered value of ac conductivity and then gradually rises with frequency. From this two distinct ac conductivity areas are identified: one with frequency-dependent nature (σ_{ac}) and a second one with frequency-independent nature (σ_{dc}) [48]. According to Jonscher's law, the formation of the plateau surface at the high-frequency region may be a result of both dc and ac conductivity in the sample whereas the development of the plateau surface at the low-frequency area may be due to a direct result of dc conductance [49]. The long-range movement of free charges in a whole path is bounded by two electrodes that provides σ_{dc}. With increase in temperature, the dc part extends owing to reduction in bound charge density. The ac part seems to be in higher-frequency range. A definite frequency of ac part (known as relaxation frequency) is found from the frequency variation of impedance plot. With increase in temperature, the relaxation frequency goes forward to the high-frequency area. These phenomena can be observed by the jump relaxation concept well known by Funke. According to Funke, a long-time successful hopping of free charge happens in the low-frequency area. This is known as the nearest-neighbor hopping among the committed ion and its nearest neighbor. The neighboring ions relax after hopping action to their region. This short-range hopping on the application of external ac field acquires an almost constant conductivity value equal

Fig. 5 (A) AC conductivity against frequency at a different temperatures, (b) AC conductivity versus 1000/T (K^{-1}) of $Ca_3Bi_2WO_9$, (c) fitted graphical curve of AC conductivity with frequency
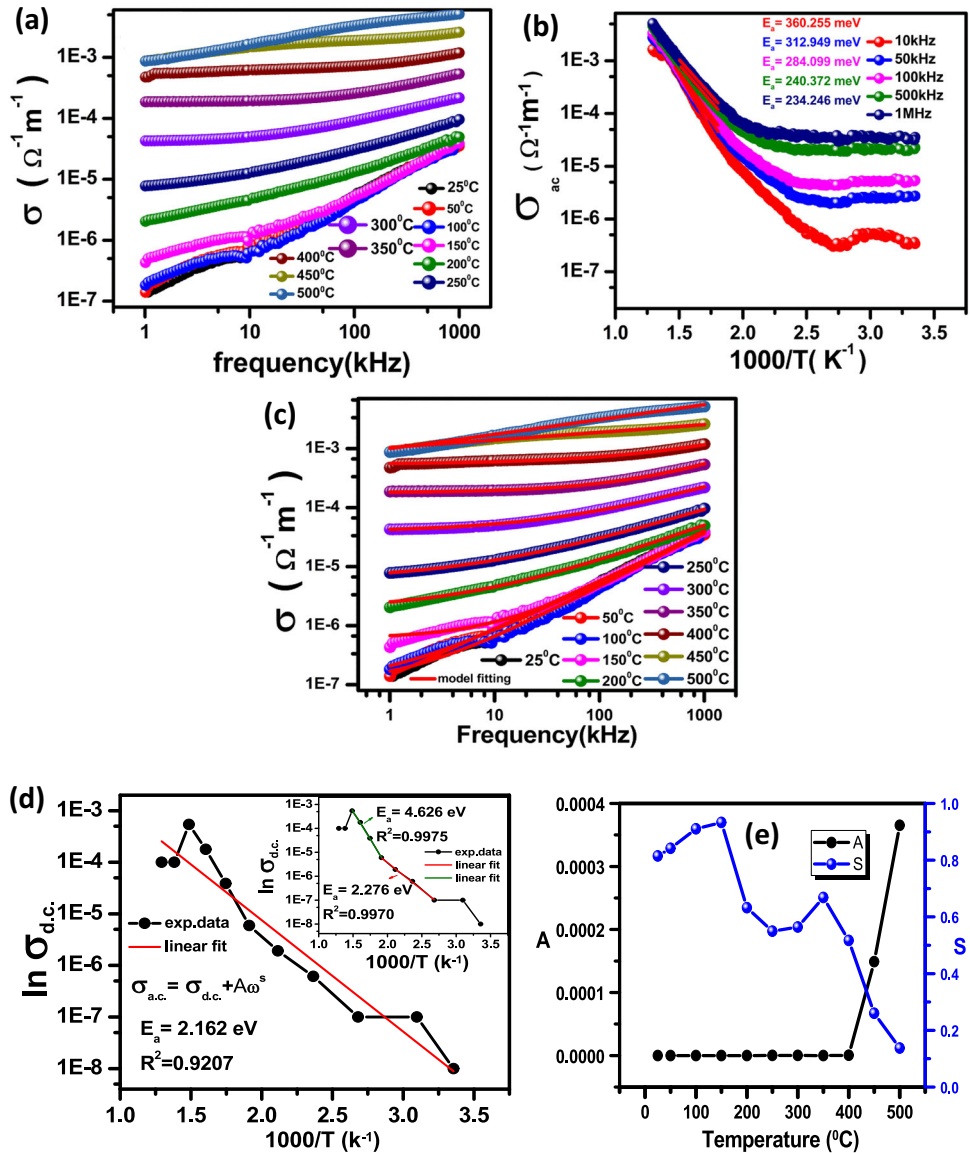

to σ_{dc}. With increase in frequency, the charges do not respond to the applied ac field; thus, backward hops happen along with specific fruitful hops that provide the dispersion of conductivity [50, 51].

Figure 5b shows a relation of the σ_{ac} vs. 1000/T at various frequencies. The activation energy is given by the slope of the linear fit to the plot. The estimated activation energies for 10 kHz, 50 kHz, 100 kHz, 500 kHz, and 1 MHz are 360.255 meV, 312.949 meV, 284.099 meV, 240.372 meV, and 234.246 meV, signifying that the relaxation mechanism is thermally activated [39]. A linear fit curve of ac conductivity vs. frequency is shown in Fig. 5 (c).

The dc conductivity (σ_{dc}) with temperature is represented in Fig. 5(d). The dc conductivity can be

evaluated from the relation $\sigma_{dc} = \sigma_0 e^{(-Ea/k_B T)}$, where σ_0 = pre-exponential factor, k_B = Boltzmann's constant = 1.38×10^{-23} J/K and E_a signifies the activation energy. The value of E_a is determined by the slope of the linear fit estimated from the plot of $\ln \sigma_{dc}$ with the inverse of absolute temperature, which is 2.162 eV in dc conduction [52]. From the fitting values, the σ_{dc} is found to increase with temperature rise. This signifies a thermally activated conduction mechanism. The calculated value of activation energy is found to be 2.276 eV and 4.626 eV in the temperature region of 373 K–523 K and 523 K–673 K, respectively, which show the activation energy differ by ignoring the high-temperature and low-temperature regions. The behavior of A (pre-exponential

Fig. 6 (A) Temperature variation of thermistor constant (β) and temperature coefficient of resistance TCR and (b) logarithm of electrical resistivity against reciprocal of temperature. d DC conductivity vs. 1000/T, (e) relation of A and s with different temperatures
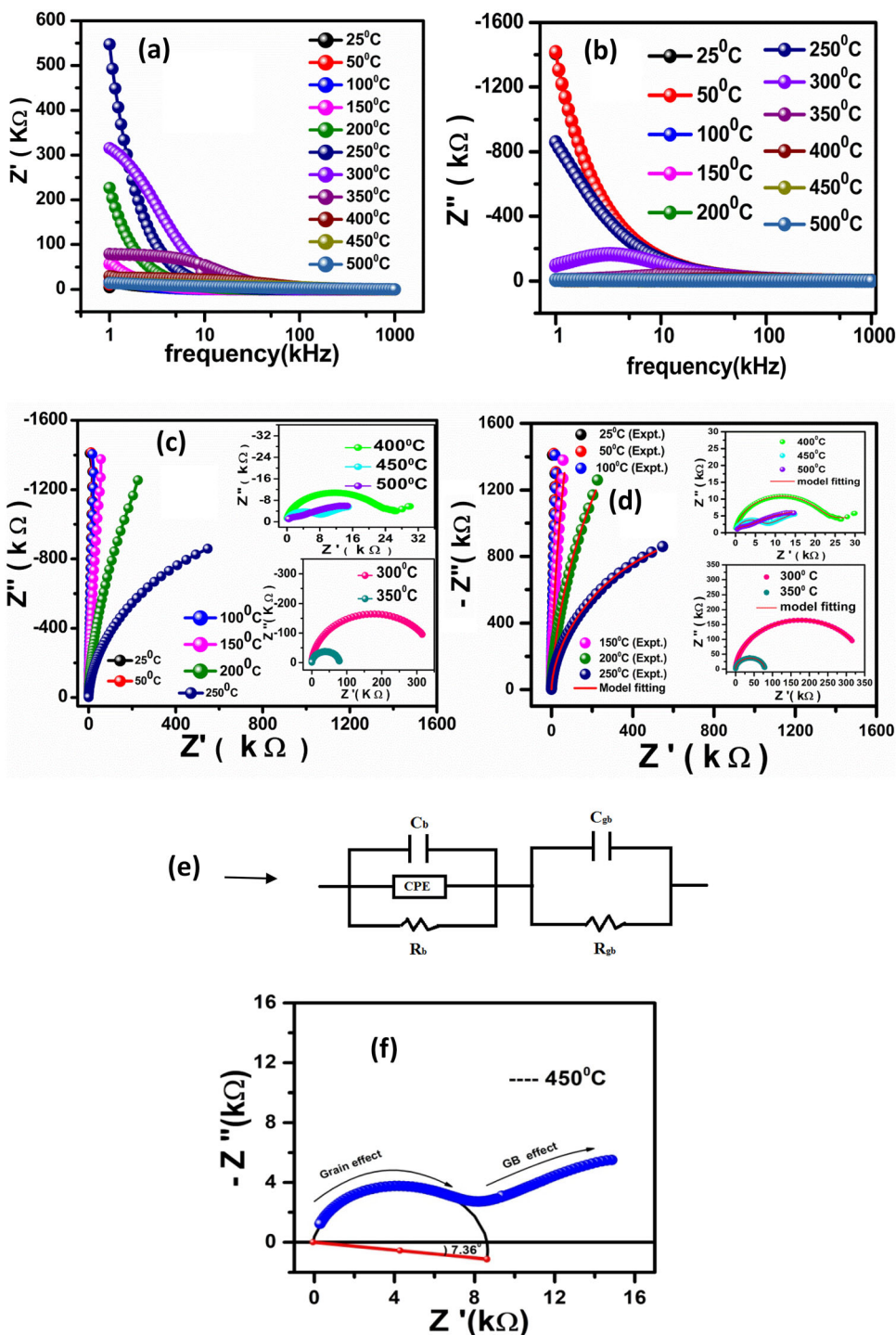
factor) and s (exponential power) at various temperatures is illustrated in Fig. 5(e). The interaction between crystal lattices and charged ions is represented by parameters. Table 2 shows the fitted electrical conductivity values. The value of s reduces as temperature increases, which is due to the hopping process. The non-linearity curve indicates that ac conductivity follows the Universal power law.

The pre-exponential parameter A determines polarization intensity, whereas the exponential parameter s analyzes the required interaction between ions of which value lies in between 0 and 1

Table 2 Value of σ_{dc}, s, A, and R^2 at different temperatures form ln σ_{dc} vs. 1000/T plot

Temperature	σ_{dc} (Ω^{-1} m^{-1})	s	A	R^2
25 °C	1E-8	0.81482	4.80485E-10	0.9969
50 °C	1E-7	0.8415	3.25651E-10	0.9976
100 °C	1E-7	0.9104	1.288E-10	0.9967
150 °C	6.13291E-7	0.93276	1.01403E-10	0.9989
200 °C	1.91117E-6	0.63219	7.78468E-9	0.9983
250 °C	5.92262E-6	0.5495	4.40339E-8	0.9995
300 °C	3.89E-5	0.56412	7.70396E-8	0.9999
350 °C	1.78465E-4	0.6684	3.6337E-8	0.9980
400 °C	5.41092E-4	0.51704	4.87956E-7	0.9989
450 °C	1E-4	0.26036	1.48883E-4	0.9992
500 °C	1E-4	0.13743	3.65258E-4	0.9991

indicating the translational motion. According to Table 2, the value of s is 0.93276 at 150 °C and declines with increasing temperature, which may be due to the existence of disorders caused by strong ionic interactions. Again, at around 500 °C, s reaches 0.13743, indicating the presence of mobile ions in the hopping process. There are several conduction methods found from s values. The first one is OLPT (overlapping large polaron tunneling) in which s value reduces to minimum weight and increases with an increase in temperature. The second one is NSPT (non-overlapping small polaron tunneling) conduction method. In this method, s value increases with the rising temperature. The third one is QMT (quantum mechanical tunneling) conduction method. In this case, the *s* value is almost equivalent to 0.8 at every temperature or else slightly increases with a rise in temperature. The fourth one is CBH (correlated barrier hopping) conduction method. In this process, the s value decreases with rising temperature [53]. In our case, variation of the s value shows the conduction mechanism to be QMT nature in the early-temperature range, later decreasing activities initiated for CBH type conduction mechanism. In QMT of electrons method, the overlapping of the wave function of the localized state occurs and electrons tunnel through the potential barrier that split up into two localized states. Electronic relaxation is observed as the cause of dielectric loss. In this method, the characteristic tunneling distance R_ω, the ac conductivity σ_{ac}, and the exponential power s obtained from σ_{ac} according to relation for a particular temperature T is specified as follows [54, 55]:

$$s(\omega, T) = \left(\frac{\partial ln(\sigma_{ac}(\omega, T))}{\partial ln(\omega)}\right)_T,$$

$$R_\omega(\omega, T) = \frac{1}{2\alpha} \ln\left(\frac{1}{\omega\tau_o}\right),$$

$$\sigma_{ac} = \frac{\pi^2}{12} \frac{e^2 K_B T}{\alpha} (g(E_F))^2 \omega R_\omega^4,$$

$$s(\omega, T) = 1 - \frac{4}{\ln\left(\frac{1}{\omega\tau_o}\right)},$$

in which α is the inverse of the localization length, $g(E_F)$ is the density of states at the Fermi level, and τ_o represents relaxation time. In CBH conduction method, small polaron/bipolaron hopping happens along the coulomb barrier that splits up defect centers. The ac conductivity, in this case, illustrated [56, 57] as follows:

$$\sigma_{ac} = \frac{n\pi^3 N N_p \varepsilon_0 \varepsilon' \omega R_\omega^6}{24},$$

in which n symbolizes polaron number (n = 1 for small polaron and n = 2 for bipolaron), N symbolizes the localized state density where polarons exist, N_P signifies the localized state density where the polarons hop, ε_0 denotes dielectric constant of free space, ε' is the dielectric constant of ceramic, and R_ω characterizes hopping distance. The relation among NN_P and R_ω can be written as follows:

$$NNp = \begin{cases} N_T^2 e^{\frac{-E_{eff}}{k_B}}, n = 1 \\ N_T^2, n = 2 \end{cases}$$

$$R_\omega = \frac{4ne^2}{\pi\varepsilon'\varepsilon_0\left[W_M - k_B T ln\left(\frac{1}{\omega\tau_0}\right)\right]},$$ in which N_T signifies the number of state density, E_{eff} denotes the effective energy in every state, and W_M signifies the extreme height of the potential barrier that must overcome the polaron restricted in localized regions. The exponential power s can be observed as follows: $s = 1 - \frac{6k_B T}{W_M - k_B T \left(\frac{1}{\omega\tau_0}\right)}$, and for a high value of $\frac{W_H}{k_B T}$,

$$s = 1 - \frac{6}{\frac{W_M}{k_B T}}.$$

Following the CBH model, a small polaron plays an important role in the conduction for $W_M = Ea/4$, and bipolaron plays a major character in the conduction for $W_M = Ea/2$, in which Ea denotes the

activation energy [56]. The Ea can be measured from the Arrhenius relation:

$$\sigma = Ae^{\frac{-E_a}{k_BT}},$$

$$\ln \sigma = \frac{-E_a}{k_BT} + \ln A.$$

The Ea value forms the plot of $\ln \sigma_{dc}$ with the inverse of temperature, which is 2.162 eV in dc conduction, and in ac conduction, its value lies between 0.234 and 0.360 at several frequencies. In a relative study, the value of Ea in the dc field is constantly found high as it is related to the large-range movement of charges and wants additional energy for the hopping method; however, in the presence of an ac field, the local forward-reverse action requires a smaller amount of energy. With the rise in frequency, Ea reduces due to an increase in space charge carriers. The range of Ea values indicates that the conduction is extrinsic electronic conduction held by the movement of oxygen vacancies with temperature [57].

3.5 Impedance analysis

Complex impedance spectroscopy is a useful process for obtaining electrical properties of materials and precise information on the microstructural. As a result, this method improves the capacity to consider the electrical characteristics of materials in terms of microstructure, crystal symmetry, grain and grain boundaries, explicit transport capabilities, and charge storage ability. The complex impedance behavior with frequency reveals the conductivity. Measurement of electrical properties at several temperatures (25–500 °C) in an extensive frequency range (1 kHz–1 MHz) was performed to improve the efficiency of the created sample. Complex electric impedance (Z*) and complex electric modulus (M*) can describe the frequency-dependent properties of ceramics. The relation between them can be derived as follows:

$$Z* = Z'(\omega) - jZ''(\omega) = R_s - \frac{j}{\omega C_s}\frac{1}{2} \text{ and}$$

$$Z''(\omega) = \frac{Z'(\omega)}{\tan \delta},$$

in which $Z'(\omega)$ and $Z''(\omega)$ are for a real and imaginary parts of complex impedance, respectively. The real part of impedance corresponds to resistance, whereas the imaginary part corresponds to reactance.

R_s is used for series resistance and C_s is used for capacitance, ω = angular frequency, and C_0 is geometrical capacitance that has a value $\frac{A\varepsilon_0}{t}$, in which A = surface area of the pellet, ε_0 permittivity of the vacuum $(8.854 \times 10^{-12} \text{F/m})$, and t = thickness of sample.

Fig. 6 Variation of (a) real part (Z′) and (b) imaginary part (Z″) with frequency in $Ca_3Bi_2WO_9$. **b** Indicates that the Z″ decreases with increasing temperature, indicating that the sample has a high conductivity. In ferroelectric at low temperatures, this pattern occurs because the relaxation processes are caused by immobile species, but at high temperatures, defects and vacancies are major sources. The temperature rise signifies the presence of a relaxation process in the prepared sample since the curves are substantially suppressed. **c** Nyquist plots, (d) Fitted Nyquist Plot of Ca3Bi2WO9 ceramic, (e) {(CQR) x (CR)} equivalent circuit. Figure 6. (f) Depression angle at 450 of $Ca_3Bi_2WO_9$.

Figure 6a depicts Z′ vs. frequency, whereas Fig. 6 (b) depicts Z″ vs. frequency at various temperatures. In the low-frequency domain, a widely dispersed value of Z′ and Z″ is seen, which monotonically declines and reaches a steady value with increasing frequency caused by the reduced contribution of space charges [58]. Z′ is strongly dependent on the frequency, which confirms the reduction in resistance as frequency increases. The decrease of Z′ with increasing temperature confirms the semiconductor characteristics or the negative temperature coefficient of resistance (NTCR) of the sample. Furthermore, in the low-frequency zone, Z′ curves decrease slowly at low temperatures whereas those with the increase of both frequency and temperature decrease distinctly and finally become frequency independent. It indicates the conducting behavior of resistive grain boundaries in the high-temperature zone [59]. At low frequencies, the independent character of Z′ explains the continued existence of dc conductivity [60]. In the low-frequency area, the hopping of charge carriers (plateau area) is known as dc resistance. The hopping happens through a grain boundary that performs as a potential barrier separating two successive grains. After the relaxation frequency, the number of space charge carriers rises and bound charge carriers decrease, which are shown in the Z′ nature in the higher-frequency area, which shows resistance to

ineffective hopping results in the relaxation of charge carriers.

The Nyquist plots of CBWO perovskite at different temperatures are indicated in Fig. 6c. The Argand plots show that with increasing temperature, the area below the complex impedance and arcs decreases, indicating the NTCR characteristic of the material and thermally activated relaxation process. The first region indicates to the grain impact that has a prominent effect in the high-frequency region. The other region seems to have the grain boundary role which has a prominent effect in the low-frequency region. The complex impedance for the compound is inscribed as follows:

$$Z^* = \frac{1}{R_g^{-1} + i\omega Q_g} + \frac{1}{R_{gb}^{-1} + i\omega Q_{gb}} = Z' + Z''$$

$$\text{where } Z = \frac{R_g}{1 + \left(\omega R_g Q_g\right)^2} + \frac{R_{gb}}{1 + \left(\omega R_{gb} Q_{gb}\right)^2} \text{ and,}$$

$$Z'' = -\left\{ R_g \left[\frac{\omega Q_g R_g}{1 + \left(\omega R_g Q_g\right)^2} \right] + R_{gb} \left[\frac{\omega Q_{gb} R_{gb}}{1 + \left(\omega R_{gb} Q_{gb}\right)^2} \right] \right\}.$$

The primary component of Z′ and Z′′ specifies the resistive portion and ac storage part of the grain. Similarly, the second component indicates the grain boundary region.

To study the significance of grain (bulk) and grain boundaries, a Nyquist plot is required in defining electrical conduction pathways. The resistance (R), capacitance (C), frequency power (n), quality factor (Q), a correction factor of grains (g) and grain boundary (gb) are estimated from Nyquist curves fitted with the ZSIMPWIN version 2.0 software code in the current study shown in Table 3. The data are estimated from the {(CQR) x (CR)} equivalent circuit shown (Fig. 6 (e)), and the fitting curve is completely coordinated, as revealed in Fig. 6 (d). Grains are highly conducting. The charge carriers move and favor to polarize in the grain boundary area which performs like a trapping perimeter and also has added capacitance value. The grain boundary capacitance is associated with the barrier layer width. The barrier layer width (ω) is directly proportional to n_b/n_f, in which n_b is the bound charge density and n_f is the free charge density which involves in hopping at the grain boundary area. As the temperature increases, n_b value decreases because of thermal depopulation. But n_f value increases as a result of thermal activation. The entire procedure reduces the value of ω with temperature increase.

The estimated depression angle in the current study is 7.36⁰ at 450°C, signifying the presence of another relaxation mechanism known as the non-Debye type of relaxation in the material.

3.6 Modulus studies

Electrical modulus research gives an appropriate understanding of relaxation mechanisms in the prepared sample, which may be comprehended from complex modulus spectroscopy. The approach is utilized to study the influence of charge carrier type, electrode polarization, relaxation process, and mobility [61–63]. At the microscopic level, the complex modulus (M*) is applied in discrete molecules to illustrate the dominance of localized charge carriers for long-range conduction mechanisms. The physical quantities can be written as follows: $\varepsilon^*(\omega) = \varepsilon'(\omega) - j\varepsilon''(\omega)$, where ε' and ε'' signify the real permittivity and imaginary permittivity, respectively. The relation among them can be derived as follows:

$$M*(\omega) = \frac{1}{\varepsilon^*} = \frac{1}{\varepsilon' - j\varepsilon''} = M' + jM'' \text{ and}$$

$$M* = \frac{\varepsilon'}{\varepsilon'^2 + \varepsilon''^2} + J\frac{\varepsilon''}{\varepsilon'^2 + \varepsilon''^2}.$$

The variation of M′ with frequency is revealed in Fig. 7 (a). The study of the M′ plot shows that the curve is S shaped and declines tend to zero, indicating the lack of the polarization effect of the electrode. The M′ curve rises with frequency and merges in the high-frequency zone, confirming the discharge of space charge polarization. The data predicated on impedance and dielectric experiments [64, 65] support this nature.

Figure 7b depicts the relation of M′′ with frequency at different temperatures. The presence of short-range or long-range mobile charges is shown by analyzing the imaginary modulus portion. In the low-frequency range, the value of M′′ approaches zero, due to electrode polarization. It is remarkable to show that M′′ increases with frequency, reaches its highest maximum value (M′′max), and then decreases. The existence of peaks in the M′′ spectra show the activation of a conduction method [66]. In the low-frequency area, the charge carriers are mobile over long distances (charge carriers show the opportunity of ion movement by jumping from one site to the neighboring site), whereas, for high

Table 3 Value of resistance, capacitance, and a correction factor of grains (g), grain boundary (gb) of $Ca_3Bi_2WO_9$

T (°C)	model	C_b (F)	Q	n	$R_b(\Omega)$	C_{gb}(F)	$R_{gb}(\Omega)$
25^0(Expt.)	(CQR) (CR)	2.132 E-009	1.772E-007	7.456E-001	1.821 E+003	1.129E-010	8.696 E+007
(Fitting)		2.133 E-009	1.769E-007	7.457E-001	1.820 E+003	1.129E-010	8.698 E+007
50^0(Expt.)	(CQR) (CR)	4.193 E-016	4.766E-008	8.526E-001	3.254 E+002	1.125E-010	7.293 E+007
(Fitting)		1.385 E-015	4.761E-008	8.527E-001	3.253 E+003	1.125E-010	7.294 E+007
100^0(Expt.)	(CQR) (CR)	3.079E-010	1.289E-007	8.030E-001	1.861 E+003	1.134E-010	6.098 E+007
(Fitting)		3.078E-010	1.289E-007	8.030E-001	1.862 E+003	1.134E-010	6.101 E+007
150^0(Expt.)	(CQR) (CR)	1.424E-014	1.932E-008	8.971E-001	6.069E+002	1.152E-010	2.887 E+007
(Fitting)		6.569E-015	1.933E-008	8.971E-001	6.064 E+003	1.152E-010	2.887 E+007
200^0(Expt.)	(CQR) (CR)	9.202E-010	5.925E-008	7.913E-001	3.173 E+004	1.232E-010	7.554 E+006
(Fitting)		9.201E-010	5.924E-009	7.913E-001	3.173 E+004	1.232E-010	7.554 E+006
250^0(Expt.)	(CQR) (CR)	4.884E-010	1.185E-010	6.425E-001	8.640 E+004	1.418E-010	1.883 E+006
(Fitting)		4.884E-010	1.186E-008	6.423E-001	8.643 E+004	1.418E-010	1.883 E+006
300^0(Expt.)	(CQR) (CR)	1.782E-010	1.734E-007	7.662E-001	2.918 E+004	2.377E-010	4.982 E+004
(Fitting)		1.793E-010	1.778E-009	7.647E-001	2.896 E+004	2.365E-010	5.003 E+004
350^0(Expt.)	(CQR) (CR)	1.583E+012	1.825E-011	3.046E-002	1.063 E+005	9.022E-009	1.552 E+003
(Fitting)		1.496E+013	4.022E-011	2.014E-002	5.065 E+004	9.022E-009	1.552 E+002
400^0(Expt.)	(CQR) (CR)	3.054E-010	5.175E-007	2.863E-001	4.675 E+004	1.778E-010	1.671 E+004
(Fitting)		3.054E-010	5.179E-006	2.862E-001	4.679 E+004	1.778E-010	1.671 E+004
450^0(Expt.)	(CQR) (CR)	2.596E-010	2.270E-006	4.093E-001	6.810 E+005	1.728E-010	5.701 E+003
(Fitting)		2.596E-010	2.268E-006	4.094E-001	6.803 E+004	1.728E-010	5.702 E+003
500^0(Expt.)	(CQR) (CR)	1.518E-012	9.153E-007	4.447E-001	3.542 E+004	2.721E-010	1.522 E+003
(Fitting)		1.518E-010	9.154E-007	4.447E-001	3.542 E+004	2.721E-010	1.522 E+003

frequencies, the carriers are restricted to potential wells. Thus, they are mobile over short distances [67–69], and they can bring up the movement of the carriers located in the wells [69]. With increase in temperature, it is observed that the peak appears to move to the high frequencies signifying the thermal activation of the relaxation time [67, 70].

Fig. 7 (A) M´ with frequency, (b) M´´ with frequency, and (c) variation of M´ with M´´ of $Ca_3Bi_2WO_9$ ceramic. Figure 7. (d) The plots of modulus (M"/ M" max) and impedance (Z'/ Z* max) as a function of frequency at 300°C, (e and f) behavior M" and Z" with frequency at 300°C and 350°C, (g) M"/M"$_{max}$ with log (f/f $_{max}$) at different temperatures and, (h) the relation of Z' and Z" with frequency at fixed temperature 300^0 C of $Ca_3Bi_2WO_9$ ceramic
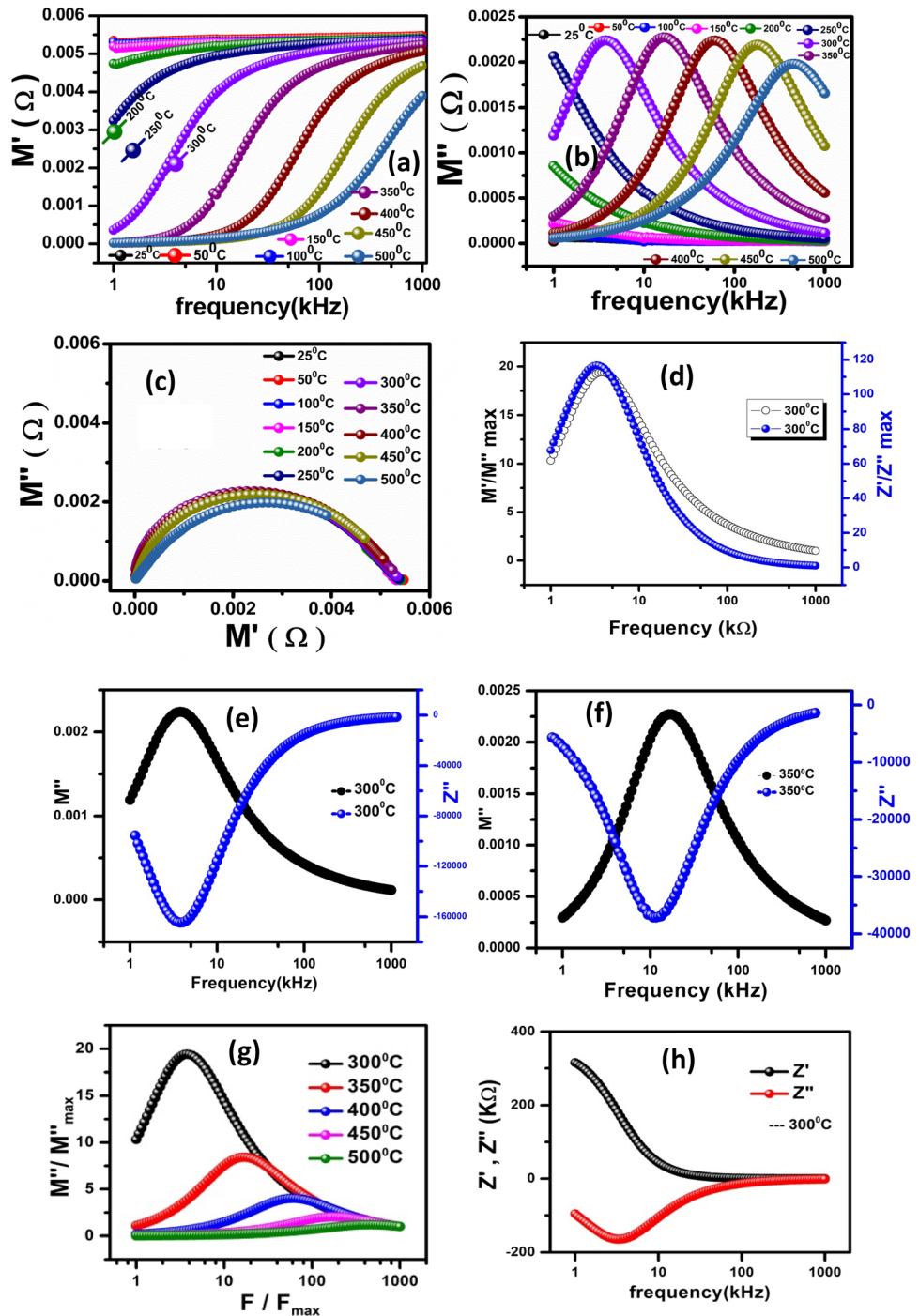
The modulus curve in Fig. 7 (c) displays irregular peaks at different frequencies. In this case, the peaks at low frequencies assist mobile ion diffusion for some path, but at high frequencies, the peaks carry mobile ions for a short range due to their confinement by a barrier well [71]. Furthermore, at the high-frequency zone, the shifting of the curve shows the non-Debye kind of relaxation mechanism and indicates the hopping mechanism as a method for explaining the conductivity process. It shows a sequence of decentered semicircles of which centers are positioned above the x-axis. These semicircles become small arcs of circles at the highest temperatures. The semicircular arc occurs at certain temperatures showing the single-phase behavior of the material [72]. The decentralization is indicative of

non-Debye relaxation and the material abides by the Cole–Cole formalism [70, 73], which goes in good consistence with the impedance data. The thermal activities of the resistance are noticeable from the curves M″ = f (M´) as with rise in temperature causes a decline in resistance. Also, it is observed that the semicircle diameter increases with temperature, which shows the increase in the capacity of the grains. This verifies the thermal activation of the conduction method in the material as the grain capacity is inversely proportional to the grain resistance [74].

According to Macdonald, the elevation of the peak varies with the inverse value of the capacitance [75]. In our study, the elevation of the peak rises with increasing temperature, indicating a lower capacitance value.

In the conductivity process, the effect of localized/delocalized charge carriers of the CBWO is explained.

Figure 7d displays the frequency with (Z″/Z″ max) and (M″/M″max) at a particular temperature. Overlapping peaks indicate the presence of a long-range charge carrier [76]. The peak behavior shows the transport mechanism, which is due to the short-range and long-range charge carriers [77]. A plot is drawn with frequency in the x-axis, M″ and Z″ in the y-axis, at 300 and 350 explained temperature, as viewed in Fig. 7 (e and f), to evaluate the stable phase factor throughout the fitting of Nyquist plots and to study the contribution of space charge polarization [78]. In the high-frequency regions, the relaxation peak associated with Z″ can be noticed, but the relaxation peak associated with M″ appears to be in a low-frequency zone. The lack of overlapping peaks indicates that the synthesized sample appears to have both localized charge carriers and long-term conductivity [79–81], which are constantly participating in the relaxation mechanism. The normalized curve of CBWO was observed by plotting the M″/M″ max vs. log (f/fmax), as shown in Fig. 7 (g). The temperature-independent active process in the sample is indicated by the overlapping of the curves [82]. Figure 7 (h) illustrates the study of the frequency dependence of the Z′ and Z″ at a fixed temperature of 300°C. It has been noted that the relaxation frequencies for Z′ and Z″ are equal and compensate for one another. In addition, these curves imply a departure from the Debye model to allow for conductivity [83].

3.7 Study of ferroelectric property

The characteristics of the (P-E) loop demonstrate the occurrence of a hysteresis loop which shows the ferroelectric behavior in the material.

An electric field with polarization known as the hysteresis loop at temperatures of 25 °C, 75 °C, 100 °C, and 125 °C is depicted in Fig. 8. It can be used to demonstrate that the substance is ferroelectric. It is generally well known that the ideal hysteresis loop depends on several factors, including the processing conditions for the material, the poling conditions, the distribution of vacancies, and the ions used as a dopant. It may be because of several factors including experimental restrictions. The hysteresis loop implies remanent polarization with a non-zero value. However, the P–E loop illustrated in Table 4 below is used to compute the coercivity field, remanent polarization, coercive field maximum (Emax), and Pmax (spontaneous polarization). As temperature rises, the value of remanence polarization and coercivity field decreases. The proper nature of P–E loop analysis implies that the studied material may have a ferroelectric phase [84] that is steady with a minor variance in our analysis. Sometimes improper loop of banana type may occur due to conductivity. Therefore, it is required to confirm the ferroelectric phase transition with other experiments.

3.8 Effect of temperature on resistance and NTC thermistor

This section discusses the temperature dependence of resistance. Figure 9 depicts the resistance behavior at temperatures ranging from 523 to 723 K. It is
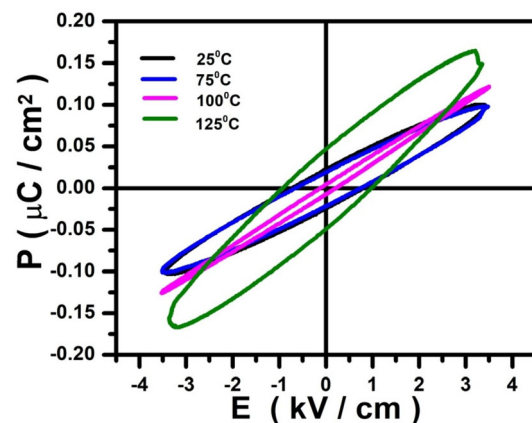

Fig. 8 The hysteresis curve of $Ca_3Bi_2WO_9$

Table 4 The value of Coercivity, Remanence, E_{max}, and P_{max} obtained from the P–E loop at different temperatures

Temp. (°C)	Coercivity (kV/cm)	Remanence (µC/cm²)	Max. electric field (E_{max}) (kV/cm)	Max. polarization (P_{max}) (µC/cm²)
25°C	011.743	000.044	023.821	000.077
50°C	005.803	000.046	012.012	000.049
75°C	011.945	000.044	026.152	000.097
100°C	008.271	000.035	026.181	000.108
125°C	002.080	000.014	026.085	000.166
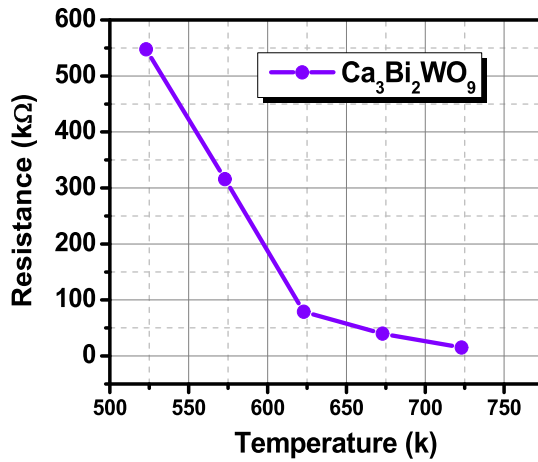
Fig. 9 Temperature-dependent resistance from 523 K–723 K

projected that when the temperature raises, the value of the resistance falls, demonstrating the negative temperature coefficient of resistance (NTCR) features [85–87].

A thermistor is a sensor device that operates on the principle of resistance variation with temperature. Thermistors are classified into two types: those that increase resistance as temperature increases and those that decrease resistance as temperature increases. The former is known as a PTC (positive temperature coefficient) thermistor, while the latter is known as an NTC (negative temperature coefficient) thermistor.

To know the working and principle of a thermistor, some physical quantities like thermistor constant (β) and temperature coefficient of resistance (TCR) are measured. The variation between resistance and thermistor constant for NTC thermistor can be calculated as $R = e^{\frac{\beta}{T}}$. The thermistor constant can be calculated from the relation:

$$\beta = \frac{\ln \frac{R_1}{R_2}}{\frac{1}{T_1} - \frac{1}{T_2}},$$

where β signifies the thermistor constant, R_1 and R_2 are the initial and final resistance, and T_1 and T_2 are the initial and final temperature, respectively. Figure 10 (a) depicts the variation of β and TCR with temperature in the current study. The linear relation between β and T supports the NTC property of the material, implying the NTC thermistor, which supports in the high-temperature region 523 K–723 K. Now, the temperature coefficient of resistance (TCR)
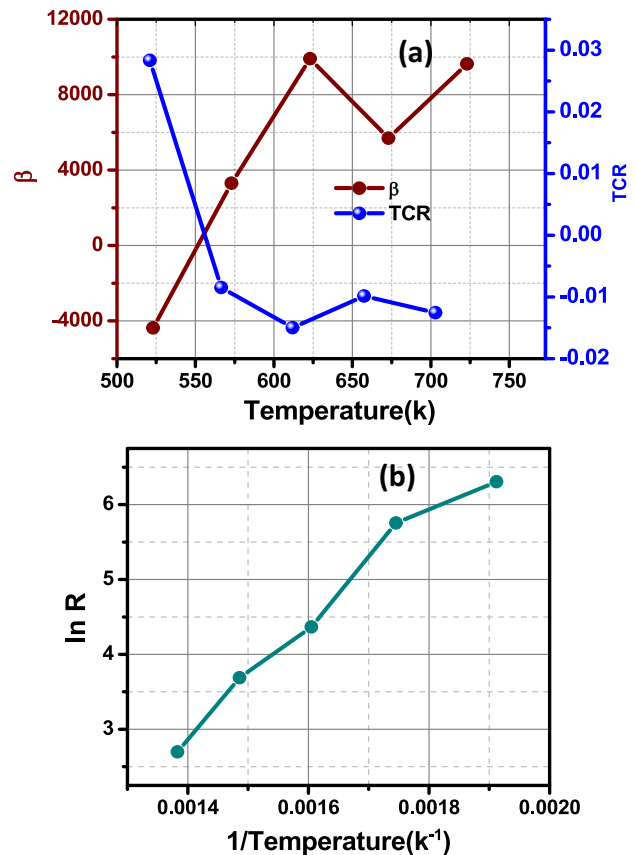

Fig. 10 (a) Temperature variation of thermistor constant (β) and temperature coefficient of resistance TCR and (b) logarithm of electrical resistivity against reciprocal of temperature.

can be measured from the relation: $TCR = \frac{1}{T_2 - T_1}$ $[\frac{R_2}{R_1} - 1]$,

where R_1 and R_2 are the initial and final resistances, T_1 and T_2 are the initial and final temperatures, respectively. Figure 6A shows temperature variation of thermistor constant (β) and temperature coefficient of resistance TCR and (b) logarithm of electrical resistivity against reciprocal of temperature.

The temperature coefficient of resistance (TCR) is generally represented as a percentage per degree centigrade (1/°C). It is observed that as temperature increases, the value of TCR decreases. The thermistor applications are strongly supported by the non-linearity curve of the TCR with temperature. Figure 6b shows the temperature dependence of resistance on an inverse of temperature. The relation between the logarithm of electrical resistivity and the inverse of temperature shows linearity. The resistivity reduces continuance as the temperature rises, showing that the sample is an excellent NTC thermistor and suitable for thermistor-based sensors [88].

4 Conclusions

The monoclinic phase of CBWO is suggested by the structural study of the samples made by a solid-state method. Average crystallite size and lattice strains are determined to be 73.29 nm and 0.0023, respectively. Correspondingly, the microstructural investigation of the synthesized sample reveals that a high-density sample with unique morphology and reduced porosity was created. The behavior of SEM characteristics shows that both large and relatively tiny grains are scattered consistently along with distinct grain boundaries. The analysis of the EDAX picture verifies the existence of each component element. The impedance spectroscopy study shows strong evidence of NTCR behavior, which is confirmed by the investigation of dielectric characteristics. While the ac conductivity indicates the presence of a thermally induced relaxation mechanism, the modulus behavior indicates the presence of non-Debye relaxation. The hysteresis loop analysis shows that the material might have ferroelectric properties yet to be confirmed by other experiments. The value temperature coefficient of resistance (TCR) and thermistor constant (β) gives a brief idea about NTC thermistor which applies to thermistor-based devices and sensors.

Author contributions

SSH: data collection, writing—original draft. DP—software, validation. RNPC: supervision, methodology, review, editing, visualization.

Data availability

The author can provide the data in the paper upon reasonable request.

Code availability

The author can provide the data in the paper upon reasonable request.

Declarations

Conflict of interest The authors attest that no known financial conflicts of interest or close personal links appear to have impacted the research provided in this paper.

References

1. B.V. Antohe, D.B. Wallace, Acoustic phenomena in a demand mode piezoelectric ink jet printer. J. Imag. Sci. Technol. **46**, 409–414 (2002)
2. Irinela Chilibon, Jose N. Marat-Mendes, Ferroelectric ceramics by sol–gel methods and applications: a review, J.

Sol. Gel Sci. Technol. (2012) 64571–64611. Doi: https://doi.org/10.1007/s10971-012-2891-7.

3. T.C. Mike Chung, A. Petchsuk, Polymers, Ferroelectric, Encyclopedia of Physical Science and Technology (Third Edition),Academic Press,(2003), 659–674,ISBN 9780122274107, https://doi.org/10.1016/B0-12-227410-5/00594-9.

4. Zenghui Liu, Hua Wu, Wei Ren, Zuo-Guang Ye, Piezoelectric and ferroelectric materials: Fundamentals, recent progress, and applications, Reference Module in Chemistry, Molecular Sciences and Chemical Engineering, Elsevier, 2022, ISBN 9780124095472, https://doi.org/10.1016/B978-0-12-823144-9.00069-8.

5. F. Wang, Q. Liu, L. Yu, Y. Wang, Multi-data source-based recycling value estimation of wasted domestic electrical storage water heater in China. Waste Manage. **140**, 63–73 (2022)

6. K.R. Kendall, C. Navas, J.K. Thomas, H.C. Zur, Loye, Recent Developments in Oxide Ion Conductors: Aurivillius Phases. Chem. Mater. **8**, 642–649 (1996). https://doi.org/10.1021/cm9503083

7. S. Zhang, B. Malič, J.F. Li et al., Lead-free ferroelectric materials: Prospective applications. J. Mater. Res. **36**, 985–995 (2021). https://doi.org/10.1557/s43578-021-00180-y

8. Moure, Alberto. 2018. "Review and Perspectives of Aurivillius Structures as a Lead-Free Piezoelectric System" *Applied Sciences* 8, no. 1: 62. https://doi.org/10.3390/app8010062.

9. B. Aurivillius Mixed bismuth oxides with layer lattices Ark. Kemi, 1 (1949), pp. 499–506.

10. Zhen Zhang, Haixue Yan, Xianlin Dong, Yongling Wang, Preparation and electrical properties of bismuth layer-structured ceramic Bi3NbTiO9 solid solution, Materials Research Bulletin, 38, Issue 2(2003) 241–248,ISSN 0025–5408,https://doi.org/10.1016/S0025-5408(02)01032-2.

11. C.A.P. de Araujo, J.D. Cuchaiaro, L.D. McMillan, "M.C. Scott and J.F. Scott", Nature 374 (1995) 627.

12. Tao, Q., Xu, P., Li, M. et al. Machine learning for perovskite materials design and discovery. npj Comput Mater 7, 23 (2021). https://doi.org/10.1038/s41524-021-00495-8.

13. B. Sun, G. Zhou, L. Sun, H. Zhao, Y. Chen, F. Yang, Y. Zhao, Q. Song, ABO3 multiferroic perovskite materials for memristive memory and neuromorphic computing. Nanoscale Horizons **6**(12), 939–970 (2021). https://doi.org/10.1039/D1NH00292A

14. Roger H. Mitchell, Mark D. Welch, Anton R. Chakhmouradian, Nomenclature of the perovskite supergroup: a hierarchical system of classification based on crystal structure and composition, Mineral. Mag. 81 (2017) 411–461.https://doi.org/10.1180/minmag.2016.080.156.

15. T. Křenek, T. Kovářík, J. Pola, T. Stich, D. Docheva, Nano and micro-forms of calcium titanate: Synthesis, properties and application, Open Ceramics,8 (2021) 100177, https://doi.org/10.1016/j.oceram.2021.100177.

16. O. Sahnoun, H. Bouhani-Benziane, M. Sahnoun, M. Driz, C. Daul, Ab initio study of structural, electronic and thermodynamic properties of tungstate double perovskites Ba2MWO6 (M = Mg, Ni, Zn). Comput. Mater. Sci. **77**, 316–321 (2013). https://doi.org/10.1016/j.commatsci.2013.04.053

17. L. Chu, W. Ahmad, W. Liu et al., Lead-Free Halide Double Perovskite Materials: A New Superstar Toward Green and Stable Optoelectronic Applications. Nano-Micro Lett. **11**, 16 (2019). https://doi.org/10.1007/s40820-019-0244-6

18. M. Kobayashi, M. Ishiib, K. Haradab, Y. Uski, H. Okuno, H. Shimizu, T. Yazawab, Scintillation and phosphorescence of PbWO4 crystals, Nucl. Instrum. Methods, A 373 (1996) 333–346. https://doi.org/10.1016/0168-9002 (95)01480–2.

19. L.S. Cavalcante, J.C. Sczancoski, J.W.M. Espinosa, J.A. Varela, P.S. Pizani, E. Longo, Photoluminescent behavior of BaWO4 powders processed in microwavehydrothermal. J. Alloys Compd. **474**, 195–200 (2009). https://doi.org/10.1016/j.jallcom.2008.06.049

20. R. Dhilip Kumar, S. Karuppuchamy, Microwave-assisted synthesis of copper tungstate nanopowder for supercapacitor applications, Ceram. Int. 40 (2014) 12397–12402. https://doi.org/10.1016/j.ceramint.2014.04.090.

21. J. Zhang, J. Pan, L. Shao, J. Shu, M. Zhou, J. Pan, Micro-sized cadmium tungstate as a high-performance anode material for lithium-ion batteries. J. Alloys Compd. **614**, 249–252 (2014). https://doi.org/10.1016/j.jallcom.2014.06.119

22. C. Anil Kumar, D. Pamu, Dielectric and electrical properties of BaWO4 film capacitors deposited by RF magnetron sputtering, Ceram. Int. 41 (2015) S296–S302. https://doi.org/10.1016/j.ceramint.2015.03.130.

23. C. Shivakumara, R. Saraf, S. Behera, N. Dhananjaya, H. Nagabhushana, Scheelitetype MWO4 (M = Ca, Sr, and Ba) nanophosphors: facile synthesis, structural characterization, photoluminescence, and photocatalytic properties. Mater. Res. Bull. **61**, 422–432 (2015). https://doi.org/10.1016/j.materresbull.2014.09.096

24. G. A. Smolensky, V. A. Bokov, V. A. Isupov, N. N. Krainik, R. E. Pasinkov, A. I. Sokolov, and N. K. Jushin, The Physics of ferroelectric phenomena. Leningrad: Science (1995) 360 p. (In Russian).

25. P. Durán-Martín, A. Castro, P. Millán, B. Jiménez, Influence of Bi-site Substitution on the Ferroelectricity of the Aurivillius Compound Bi2SrNb2O9. J. Mater. Res. **13**(9), 2565–2571 (1998). https://doi.org/10.1557/JMR.1998.0358

26. S.M. Blake, M.J. Falconer, M. McCreedy, P. Lightfoot, Cation disorder in ferroelectric Aurivillius phases of the type

Bi2ANb2O9(A=Ba, Sr, Ca). J. Mater. Chem. **7**(8), 1609–1613 (1997). https://doi.org/10.1039/A608059F

27. Jae-Hyun Park, Patrick M. Woodward, Synthesis, structure and optical properties of two new Perovskites: Ba2Bi2/3TeO6 and Ba3Bi2TeO9, International Journal of Inorganic Materials 2, no. 1 (2000) 153–166 https://doi.org/10.1016/S1466-6049(99) 00071–9.

28. A. Moure, L. Pardo, Microstructure and texture dependence of the dielectric anomalies and dc conductivity of Bi3TiNbO9Bi3TiNbO9 ferroelectric ceramics, Journal of Applied Physics 97, (2005) 084103; https://doi.org/10.1063/1.1865313.

29. Y. Wang,Y. Sui, P. Ren, Wang, L. Wang, X. Wang, Su Wenhui, and Hongjin Fan, Strongly correlated properties and enhanced thermoelectric response in Ca3Co4− x M x O9 (M= Fe, Mn, and Cu) Chemistry of Materials 22(3) 2010 pp.1155–1163 https://doi.org/10.1021/cm902483a.

30. X. Xie, Z. Zhou, T. Chena, R. Liang, X. Dong, Enhanced electrical properties of NaBi modified CaBi2Nb2O9-based Aurivillius piezoceramics via structural distortion. Ceram. Int. **45**, 5425–5430 (2019). https://doi.org/10.1016/j.ceramint.2018.11.244

31. Hepeng Wang, Xiangping Jiang, Chao Chen, Xiaokun Huang, Xin Nie, Li Yang, Wenying Fan, Shaotian Jie, Hui Wang, Structure and electrical properties of Ce-modified Ca1-xCexBi2Nb1.75(Cu0.25W0.75)0.25O9 high Curie point piezoelectric ceramics, Ceramics International, 46 (2022) 1723–1730 https://doi.org/10.1016/j.ceramint.2021.09.251.

32. A. Altomare, C. Cuocci, C. Giacovazzo, A. Moliterni, R. Rizzi, N. Corriero, A. Falcicchio, J. Appl. Cryst. **46**, 1231–1235 (2013)

33. Rajanikanta Parida Parida, Bichitrananda Parida, Ranjan Kumar Bhuyan, Santosh Kumar Parida, Structural, mechanical and electric properties of La doped BNT-BFO perovskite ceramics. Ferroelectrics **571**, 162–174 (2021). https://doi.org/10.1080/00150193.2020.1853751

34. F Marinello and A Pezzuolo 2019 *IOP Conf. Ser.: Earth Environ. Sci.* 275 012011.

35. Rovani, A. C., Kouketsu, F., da Silva, C. H., &Pintaude, G. (2018). Surface characterization of three-layer organic coating applied on AISI 4130 steel. Advances in Materials Science and Engineering, 2018.

36. Yuwei Huang, Kangning Wu, Zhaoliang Xing, Chong Zhang, Xiangnan Hu, Panhui Guo, Jingyuan Zhang, Jianying Li, Understanding the validity of impedance and modulus spectroscopy on exploring electrical heterogeneity in dielectric ceramics, Journal of Applied Physics (2019), 125 (8), 084103. https://doi.org/10.1063/1.5081842.

37. S.S. Ashima, Ashish Agarwal, Reetu, Neetu Ahlawat, Monica, Structure refinement and dielectric relaxation of M-type Ba, Sr, Ba-Sr, and Ba-Pb hexaferrite. J. Appl. Phys. **112**, 14110–14115 (2012). https://doi.org/10.1063/1.4734002

38. Wu, K., Huang, Y., Li, J. and Li, S., 2017. Space charge polarization modulated instability of low frequency permittivity in CaCu3Ti4O12 ceramics. Applied Physics Letters, 111(4), p.042902. https://doi.org/10.1063/1.4995968.

39. S.K. Parida, R.N.P. Choudhary, Preparation method and cerium dopant effects on the properties of BaMnO3 single perovskite. Phase Transitions **93**, 981–991 (2020). https://doi.org/10.1080/01411594.2020.1817451

40. J. Liu, C.G. Duan, W.N. Mei, R.W. Smith, J.R. Hardy, Dielectric properties and Maxwell-Wagner relaxation of compounds ACu3Ti4O12 (A= Ca, Bi2/3, Y2/3, La2/3). J. Appl. Phys. **98**, 093703 (2005)

41. I. Ahmad, M.J. Akhtar, M. Younas, M. Siddique, M.M. Hasan, Small polaronic hole hopping mechanism and Maxwell-Wagner relaxation in NdFeO3. J. Appl. Phys. **112**, 074105 (2012)

42. A. Karmakar, S. Majumdar, A.K. Singh, S. Giri, Intragrain electrical inhomogeneities and compositional variation of static dielectric constant in LaMn1–xFexO3. J. Phys. D Appl. Phys. **42**, 092004 (2009)

43. Y. Leyet, F. Guerrero, J.P. de la Cruz, Relaxation dynamics of the conductive processes in BaTiO3 ceramics at high-temperature. Mater. Sci. Eng. B. **171**, 127–132 (2010)

44. M. Amin, H.M. Rafique, M. Yousaf, S.M. Ramay, S. Atiq, Structural and impedance spectroscopic analysis of Sr/Mn modified BiFeO3 multiferroics. J. Mater. Sci. **27**, 11003–11011 (2016). https://doi.org/10.1007/s10854-016-5216-8

45. Dhiren K. Pradhan, Shalini Kumari, Venkata S. Puli, Proloy T. Das, Dilip K. Pradhan, Ashok Kumar, J.F. Scott, Ram S. Katiyar, Correlation of dielectric, electrical and magnetic properties near the magnetic phase transition temperature of cobalt zinc ferrite, Phys. Chem. Chem. Phys. 19 (2017) 210–216. https://doi.org/10.1039/C6CP06133H.

46. J. Ross Macdonald, Comparison of the universal dynamic response power-law fitting model for conducting systems with superior alternative models, Solid State Ionics 133 (2000) 79–97 https://doi.org/10.1016/S0167-2738(00)00737-2.

47. R. Kumari, N. Ahlawat, A. Agarwal, S. Sanghi, M. Sindhu, N. Ahlawat, Phase transformation and impedance spectroscopic study of Ba substituted Na0.5Bi0.5TiO3 ceramics, J. Alloys Compd. 676 (2016) 452–460 https://doi.org/10.1016/j.jallcom.2016.03.088.

48. Subrat Kumar Barik, Suhel Ahmed, Sugato Hajra, Studies of dielectric relaxation and impedance analysis of new electronic material: (Sb1/2Na1/2)(Fe2/3Mo1/3)O3. Appl. Phys. A **125**, 200–208 (2019). https://doi.org/10.1007/s00339-019-2496-x

49. M. Yildirim, A. Kocyigit, A systematic study on the dielectric relaxation, electric modulus and electrical conductivity of Al/Cu: tiO2=N-Si (Mos) structures/capacitors. Surface Rev. Lett. **27**, 1950217–1950312 (2020). https://doi.org/10.1142/S0218625X19502172

50. B. Panda, K.L. Routray, D. Behera, Studies on conduction mechanism and dielectric properties of the nano-sized $La_{0.7}$-$Ca_{0.3}MnO_3$ (LCMO) grains in the paramagnetic state. Physica B Condens. Matter 583, 411967 (2020)

51. K. Funke, Jump relaxation in solid electrolytes. Prog. Solid. State Ch. **22**, 111–195 (1993)

52. D.C. Sinclair, A.R. West, Impedance and modulus spectroscopy of semiconducting BaTiO3 showing positive temperature coefficient of resistance. J. Appl. Phys. **66**, 3850–3856 (1989). https://doi.org/10.1063/1.344049

53. Ben Taher, Y., A. Oueslati, N. K. Maaloul, K. Khirouni, and M. Gargouri. "Conductivity study and correlated barrier hopping (CBH) conduction mechanism in diphosphate compound." *Applied Physics A* 120 (2015): 1537–1543.

54. S.R. ElliotAdv, Phys. **36**, 135 (1987)

55. A. GhoshPhys, Rev. B **41**, 1479 (1990)

56. S. Hajlaoui, I. Chaabane, K. Guidara, Conduction mechanism model, impedance spectroscopic investigation and modulus behavior of the organic-inorganic [(C3H7)4 N][SnCl5(H2O)]•2H2O compound. RSC Adv. **6**, 91649–91657 (2016)

57. Stumpe, R., Wagner, D. and Bäuerle, D., 1983. Influence of bulk and interface properties on the electric transport in ABO3 perovskites. *physica status solidi (a)*, 75(1), pp.143–154.

58. T. Md, M. Rahman, C.V. Vargas, Ramana, structural characteristics, electrical conduction and dielectric properties of gadolinium substituted cobalt ferrite. J. Alloys Compd. **617**, 547–562 (2014). https://doi.org/10.1016/j.jallcom.2014.07.182

59. K. Parida, S.K. Dehury, R.N.P. Choudhary, Structural, electrical and magnetoelectric characteristics of BiMgFeCeO6 ceramics. Phys. Lett. **380**, 4083–4091 (2016). https://doi.org/10.1016/j.physleta.2016.10.022

60. P. Ganga Raju Achary, R.N.P. Choudhary, S.K. Parida, Investigation of structural and dielectric properties in polycrystalline PbMg1/3 Ti1/3W1/3O3 tungsten perovskite, Spin 10 (2020), 2050021–10.

61. D.L. Rocco, A.A. Coelho, S. Gama, M. de C. Santos, Dependence of the magnetocaloric effect on the A-site ionic radius in isoelectronic manganites, J. Appl. Phys. 113 (2013), 113907 https://doi.org/10.1063/1.4795769.

62. P. Gogoi, P. Srinivas, P. Sharma, D. Pamu, Optical, dielectric characterization and impedance spectroscopy of Ni-substituted MgTiO3 thin films. J. Electron. Mater. **45**, 899–909 (2016). https://doi.org/10.1007/s11664-015-4209-3

63. I. Coondoo, N. Panwar, A. Tomar, A.K. Jha, S.K. Agarwal, Impedance spectroscopy and conductivity studies in SrBi2(Ta1-xWx)2O9 ferroelectric ceramics. Phys. B **407**, 4712–4720 (2012). https://doi.org/10.1016/j.physb.2012.09.024

64. H. Saghrouni, S. Jomni, W. Belgacem, N. Hamdaoui, L. Beji, Physical and electrical characteristics of metal/Dy2O3/p-GaAs structure. Phys. B **444**, 58–64 (2014). https://doi.org/10.1016/j.physb.2014.03.030

65. F.S. Moghadasi, V. Daadmehr, M. Kashf, Characterization and the frequencythermal response of electrical properties of Cu nano ferrite prepared by sol-gel method. J. Magn. Magn Mater. **416**, 103–109 (2016). https://doi.org/10.1016/j.jmmm.2016.05.012

66. T.P. Bharti, Sinha, Solid. Stat Sci. **12**, 498 (2010)

67. T.P. Dutta, Sinha. Phys. B **405**, 1475 (2010)

68. MBakr Mohamed, H. Wang, H. Fuess. Phys D: Appl. Phys. 43 (2010) 409–455.

69. E. Omri, M. Dhahri, L.C.C. Es-Souni, J. Alloys Compd. **497**, 173 (2012)

70. R. Ranjan, R. Kumar, N. Kumar, B. Behera, R.N.P. Choudhary, J. Alloys Compd. **509**, 6388 (2011)

71. S. Pattanayak, B. Parida, P.R. Das, R.N.P. Choudhary, Impedance spectroscopy of Gd-doped BiFeO3 multiferroics. Appl. Phys. A **112**, 387–395 (2013). https://doi.org/10.1007/s00339-012-7412-6

72. W. Hzez, H. Rahmouni, E. Dhahri, K. Khirouni, J. Alloys Compd. **725**, 348 (2017)

73. E. Barsoukov, J. Ross Macdonald, Impedance Spectroscopy Theory, Experiment and Applications, second ed., Wiley Interscience, New York. (2005).

74. J. Liu, C.G. Duan, W.G. Yin, W.N. Mei, R.W. Smith, Chemphys **119**, 2812 (2003)

75. S.A. Jawad, A.S. Abu-Surrah, M. Maghrabi, Z. Khattari, Electric impedance study of elastic alternating propylene–carbon monoxide copolymer (PCO-200). Phys. B **406**, 2565–2569 (2011). https://doi.org/10.1016/j.physb.2011.03.069

76. P. Ganga Raju Achary, R.N.P. Choudhary, S.K. Parida, Structure, electric and dielectric properties of PbFe1/3Ti1/3W1/3O3 single perovskite compound, Process. Appl. Ceram. 14 (2020) 146–153 https://doi.org/10.2298/PAC2002146A.

77. M. Anjidania, H.M. Moghaddama, R. Ojani, Binder-free MWCNT/TiO2 multilayer nanocomposite as an efficient thin interfacial layer for photoanode of the dyesensitized solar cell. Mater. Sci. Semicond. Process. **71**, 20–28 (2017). https://doi.org/10.1016/j.mssp.2017.05.036

78. F. Aziza, N. Gupta, G.G. Sonic, K.K. Kushwah, Contrasting effects of mismatch strain on the magnetic behavior of undoped and doped BaFeO3-δ thin films. J. Magn. Magn Mater. **517**, 167338–167347 (2021). https://doi.org/10.1016/j.jmmm.2020.167338

79. W. Yang, S. Yu, R. Sun, S. Ke, H. Huang, R. Du, Electrical modulus analysis on the Ni/CCTO/PVDF system near the percolation threshold. J. Phys. D Appl. Phys. **44**, 475305–475314 (2011). https://doi.org/10.1088/0022-3727/44/47/475305

80. D.K. Pradhan, R.N.P. Choudhary, C. Rinaldi, R.S. Katiyar, Effect of Mn substitution on electrical and magnetic properties of Bi0.9La0.1FeO3, J. Appl. Phys. 106 (2009) 24102–24106 https://doi.org/10.1063/1.3158121.

81. B.K. Barick, K.K. Mishra, A.K. Arora, R.N.P. Choudhary, D.K. Pradhan, Impedance and Raman spectroscopic studies of (Na0.5Bi0.5)TiO3, J. Phys. D 44 (2011) 355402–355410 https://doi.org/10.1088/0022-3727/44/35/355402.

82. S. Thakur, R. Rai, I. Bdikin, M.A. Valente, Impedance and modulus spectroscopy characterization of Tb modified Bi0.8A0.1Pb0.1Fe0.9Ti0.1O3 ceramics, Mater. Res. 19 (2016) 1–8 https://doi.org/10.1590/1980-5373-MR-2015-0504.

83. M. Selvasekarapandian, Vijaykumar, The ac impedance spectroscopy studies on LiDyO2 Mater. Chem. Phys. **80**, 29–33 (2003). https://doi.org/10.1016/S0254-0584(02)00510-2

84. Ajeet Kumar, K.C.James Raju, Jungho Ryu, A.R. James; Composition dependent Ferropiezo hysteresis loops and energy density properties of mechanically activated (Pb1−xLax) (Zr0.60Ti0.40)O3 ceramics, Appl. Phys. A 126 (2020) 1–10 https://doi.org/10.1007/s00339-020-3356-4.

85. C.C. Wang, S.A. Akbar, W. Chen, J.R. Schorr, High-temperature thermistors based on yttria and calcium zirconate. Sensor. Actuator. A **58**, 237–243 (1997)

86. J. Zhao, L. Li, Z. Gui, Influence of lithium modification on the properties of Y doped Sr0.5Pb0.5TiO3 thermistors, Sens. Actuators, A 95 (2001) 46–50.

87. S. Sahoo, Negative temperature coefficient resistance of CaTiO3 for thermistor application. Trans. Electr. Electron. Mater. **21**, 91–98 (2020)

88. S. Sahoo, S.K.S. Parashar, S.M. Ali, CaTiO3 nano ceramic for NTCR thermistor-based sensor application. Journal of Advanced Ceramics **3**(2), 117–124 (2014)